WILEY

RESEARCH ARTICLE

New dynamic-inflow engineering models based on linear and nonlinear actuator disc vortex models

Wei Yu[1] | Delphine Tavernier[1] | Carlos Ferreira[1] | Gijs A. M. van Kuik[1] | Gerard Schepers[2]

[1]Faculty of Aerospace Engineering, Delft University of Technology, Delft, The Netherlands

[2]Wind Energy, ECN part of TNO, Petten, The Netherlands

Correspondence

Wei Yu, Faculty of Aerospace Engineering, Delft University of Technology, Kluyverweg 1, 2629 HS, Delft, The Netherlands.
Email: W.Yu@tudelft.nl

Abstract

Two new engineering models are presented for the aerodynamic induction of a wind turbine under dynamic thrust. The models are developed using the differential form of Duhamel integrals of indicial responses of actuator disc type vortex models. The time constants of the indicial functions are obtained by the indicial responses of a linear and a nonlinear actuator disc model. The new dynamic-inflow engineering models are verified against the results of a Computational Fluid Dynamics (CFD) model and compared against the dynamic-inflow engineering models of Pitt-Peters, Øye, and Energy Research Center of the Netherlands (ECN), for several load cases. Comparisons of all models show that two time constants are necessary to predict the dynamic induction. The amplitude and phase delay of the velocity distribution shows a strong radial dependency. Verifying the models against results from the CFD model shows that the model based on the linear actuator disc vortex model predicts a similar performance as the Øye model. The model based on the nonlinear actuator disc vortex model predicts the dynamic induction better than the other models concerning both phase delay and amplitude, especially at high load.

KEYWORDS

actuator disc, CFD, dynamic inflow, engineering model, vortex model

1 | INTRODUCTION

Dynamic inflow (sometimes referred to as dynamic wake) is the phenomenon that describes the unsteady effect of the wake induced velocity in the wind turbine rotor plane due to variations in rotor load. These variations in rotor load can be caused by, eg, changes in wind speed, pitch angle, or rotor speed. The dynamic inflow effect is implicitly included in high-fidelity models, but also computationally expensive CFD or free vortex wake methods. The effect is, however, not included in the steady blade element momentum (BEM) method, which, due to its efficiency, is required for the extremely demanding calculation of a wind turbine design load spectrum with more than a million time steps, each requiring a full aero-elastic calculation of inflow, rotor, and wake. This is explained in Schepers,[1] where it is also explained that dynamic inflow can have an important impact on fatigue loads of pitch controlled wind turbines and on the design of a pitch control algorithm.[2] For this reason, much effort was spent on developing so-called engineering methods for dynamic inflow in the past decades, see, eg, Snel and Schepers[3] and Schepers and Snel.[4] The term "engineering method" refers to a simplified and transparent model for a complex physical phenomenon with a calculational effort that is acceptable for industrial wind turbine design calculations. In Schepers,[1] it is explained that most engineering models for dynamic inflow add a first-order time derivative on the axial induced velocity to the steady momentum theory relation, ie,

$$\tau du_i/dt + 4u_i(1 - u_i) = V_w C_t, \tag{1}$$

with τ a time constant. Hence, Equation (1) represents a time delay in axial induced velocity (u_i) from a change in axial force, where in the equilibrium situation Equation (1) returns to the steady momentum equation:

$$C_t = 4a(1-a), \tag{2}$$

where a is the axial induction factor. It is noted that a similar equation can be derived for the in-plane component of the induced velocity in response to variations in rotor shaft torque, but most studies (including the present one) focus on the more important axial induced velocity changes in response to variations in thrust.

The main uncertainty in all dynamic inflow research until now is found to be in the formulation of τ for which different approximations and dependencies are derived as explained below. These dependencies make that although τ is often referred as time constant, it is not a real constant but a function with dependencies on, eg, time or radial position.

Often used dynamic inflow models are the Pitt-Peters model, the Øye model, and the ECN model. The Pitt-Peters model[5] was developed based on the concept of "apparent mass." It assumes that the uniform induced velocity of the initial flow field is analogous to the flow field produced by an impermeable disc moving normal to its plane. However, the model was proposed for helicopters, whose operational conditions are different from those of wind turbines. The engineering model of Øye[6] was developed using a vortex ring model.[7] The wake expansion is determined from continuity of mass flow using the velocity at a certain location inside the wake. It results in two constants. The ECN model[1,3] was developed based on a simplified linear actuator disc model using prescribed convection velocity. The resulting time constant is a function of radial position with the shortest time scale near the tip (in view of the closer vicinity to the tip vortex). A verification against numerical results of a free wake vortex model further showed that these dynamic-inflow engineering models underestimate the phase delay of the dynamic induction for certain load cases.[8,9]

Pirrung and Madsen[10] explained why it is better to use two time constants in Equation (1). The first time constant reflects the velocity delay induced by the (very) near wake (until 0.75D behind the rotor) where there is a strong dependency of distance to the tip vortex along the blade radial position. The second (slower) time constant is invariant with blade radial position and reflects the delay in velocity induced by the "far" wake where the distance to the tip vortex is relatively insensitive to the radial position. This approach made it possible to solve some unanswered questions on the dynamic inflow time scale from Schepers.[1] It is noted that the engineering model of Øye[6] included two time constants already.

In this paper, a fundamental new approach is proposed to account for the time scale of dynamic induction using vortex models. The innovative aspect lies in the fact that it is derived from Wagner's model,[11] a model that until now was applied for 2-D unsteady airfoil aerodynamics only. Another unique aspect of the present model lies in the very thorough verification of the new approach with high-fidelity models.

The paper is structured as follows. In Section 2.1, the induction of an actuator disc under dynamic load is described, the flow decay functions are obtained from a linear and a nonlinear actuator disc vortex model. A nonlinear model takes wake expansion into account, while a linear model does not. The indicial flow field responses, describing the velocity transient at the disc due to a unit step change of the thrust, of the linear actuator disc model are obtained by a vortex tube model (VTM).[12] In the nonlinear model, the indicial flow field responses are obtained by a free wake vortex ring (FWVR) model.[8] In order to use these responses in a numerical time-marching code (eg, BEM), the indicial responses are represented by an exponential approximation. This is explained in Section 2.2. The coefficients of the exponential equations are found to be a function of radius and a function of baseline thrust (the thrust before the step change), as presented in Section 2.3. When the indicial functions are known, the resulting flow field of any given thrust input can be calculated directly using Duhamel integral of these functions. This is elaborated in Section 2.4. Further, the new models are verified by comparing the induction at the actuator disc with the numerical results of a CFD model. The CFD model, the load cases used for verification, and the analysis method are given in Section 3. The comparison of the induction from the new models and from the engineering models of Pitt-Peters, Øye, and ECN against the CFD results are presented in Section 4. The verification focuses on the amplitude and phase delay of the dynamic induction. Finally, conclusions are drawn in Section 5.

The appendices give some background on the model development and its accuracy. The dynamic-inflow engineering models of Pitt-Peters, Øye, and ECN are described in Appendix A. The effect of using a different number of exponential terms to approximate the indicial functions is discussed in Appendix B. Appendix C shows how the relationship between the coefficients of the indicial functions, the radial position, and the baseline thrust is obtained, and analyses the quality of the polynomial representation of the coefficients from the linear and the nonlinear actuator disc models.

2 | METHOD

2.1 | The induction of an actuator disc

The method assumes the flow to be incompressible, inviscid, axisymmetric, and irrotational everywhere except for the vorticity surface. As such, the loads are uniform in radial direction and hence vorticity is only shed at the edge of the actuator disc. Circulation is assumed to be azimuthally constant. The induced velocity field of an actuator disc with an arbitrarily oscillating load can be calculated from the vortex system as represented in Figure 1. The strength of the vorticity shed into the wake varies with the varying load. The wake, as a tube surface with varying strength and expansion, extends from the edge of the disc to infinity. The newly shed wake is generated at the edge of the disc and convected downstream by the local velocity. By applying the equation of velocity induced by a finite vortex cylinder derived in Branland and Gaunaa,[13] the axial velocity at a position (z_p, r_p) induced by the wake vorticity system can be calculated by the following integral:

$$\Phi(z_p, r_p, t) = \int_0^\infty \frac{-\gamma_t(z,t)}{4\pi\sqrt{r_p R(z,t)}} \left[(z-z_p)m \left(K(m^2) + \frac{R(z,t) - r_p}{R(z,t) + r_p} \Pi(m_0^2, m^2) \right) \right]_z^{z+dz}, \tag{3}$$

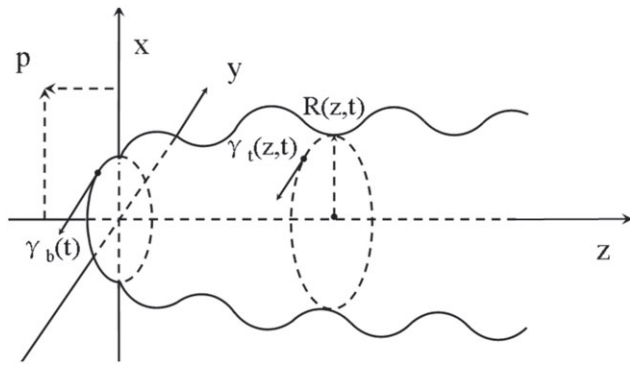**FIGURE 1** Mathematical model of an actuator-disc model with harmonically oscillating load

where $< z_p, r_p >$ are the coordinates of point P where the velocity is to be calculated, $\gamma_t(z, t)$ is the tangential vorticity of the surface at location z at time t. $K(m^2)$, and $\Pi(m_0^2, m^2)$ are the complete elliptic integrals of the first and third kind. The two elliptic parameters are

$$m^2 = \frac{4r_p R(z, t)}{(z - z_p)^2 + (R(z, t) + r_p)^2}, \tag{4}$$

$$m_0^2 = \frac{4r_p R(z, t)}{(R(z, t) + r_p)^2}. \tag{5}$$

Unsteady aerodynamic forces of an airfoil in potential flow conditions are usually described by the indicial formulations in the time domain, as reported in Beddoes[14] and Leishman.[15] The method is applied to an actuator disc here. The indicial functions are obtained instead of directly finding an analytical solution for Equation (3). Here, the indicial function refers to the (normalized) time response of the axial induction when the disc thrust jumps up or down from a baseline value to another constant value. To create a database of indicial flow field responses, two models are used: (a) a linear and (b) a nonlinear actuator disc vortex model. A series of dynamic load cases are calculated using the linear actuator disc model (the VTM) and the nonlinear actuator disc model (the FWVR model). The baseline thrust coefficients (C_t) range from 0 to 1, with a thrust change $\delta C_t = \pm 0.1$. Note that the linear actuator disc model is mainly considered to act as a benchmark for models that are also based on a linear actuator-disc model, eg, the ECN model.

In the linear VTM,[12] the classical actuator disc model is considered as a superposition of a semi-infinite vortex tube with a series of finite vortex tubes. This model resembles the model developed by Branlard and Gaunaa,[16] though a different convection velocity was investigated in Yu, Ferreira, and van Kuik.[12] The strength of the vortex tube is determined by the load on the disc. The vortex tubes are convected at the combined speed of the incoming flow and an approximated induced velocity. No wake expansion is taken into account in this linear actuator disc model.

In the nonlinear FWVR model,[8] the near wake is modeled as dynamic surfaces consisting of free vortex rings shed from the edge of the actuator disc. The far wake is represented by a semi-infinite cylindrical vortex tube. The vortex rings are considered thin, axisymmetric, and uniform. In this axisymmetric loaded actuator disc study, vortex rings expand or contract, while their central axis always coincides with the axis of the actuator disc. A cut-off scheme is used to remove singularities. No viscous diffusion or turbulence is considered in the model. The Lagrangian formulation of this model is particle based without an underlying grid. A time step of $\Delta\tau = 0.02$ and a cut-off radius of $\delta = 1 \times 10^{-5}$ are chosen for the simulations. The vortex rings are convected downstream at a combined speed of the incoming flow and the local induced velocity by the vortex system. The positions of the vortex rings are updated using a second-order Euler method. As such, wake expansion is thus considered in this nonlinear actuator disc model.

2.2 | Indicial functions

The indicial responses for the various dynamic load cases, calculated using the linear and nonlinear actuator disc vortex models, are approximated by indicial functions. These indicial functions are chosen to be represented by exponential approximations. An exponential approximation was already used before for an unsteady airfoil, eg, the exponential representation of the Wagner function[17] or the indicial lift functions of an airfoil.[14]

The normalized radially distributed axial induction at the actuator disc is denoted as $\Phi_d(r_j, t)$ and described according to Equation (6)

$$\Phi_d(r_j, t) = 1 - \beta_j e^{\omega_j^1 t} - (1 - \beta_j)e^{\omega_j^2 t}, \tag{6}$$

where the subscript j represents the radial position and the time is nondimensionalized with V_0/R. It is normalized to the induced velocity difference of the two steady states before and after load change. Note that the exponential approximation is using two exponential terms. It is shown to be better than using one or three, which is consistent with the recommendations from Pirrung and Madsen.[10] The effect of using a different number of exponential terms to approximate the indicial functions is discussed further in Appendix B. In this paper, only the approximation of the induced velocity at the actuator disc is investigated, because the induction on the actuator disc is of most interest. The induction at other locations can be dealt with in the same way.

FIGURE 2 Φ_d calculated by the vortex tube model (VTM) and the exponential approximation for baseline $C_t = 0.4$. LI, load increase case; LD, load decrease case [Colour figure can be viewed at wileyonlinelibrary.com]
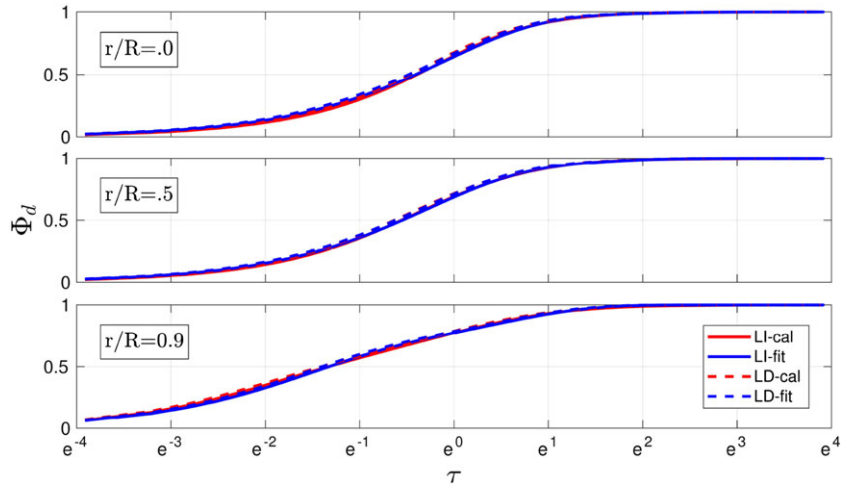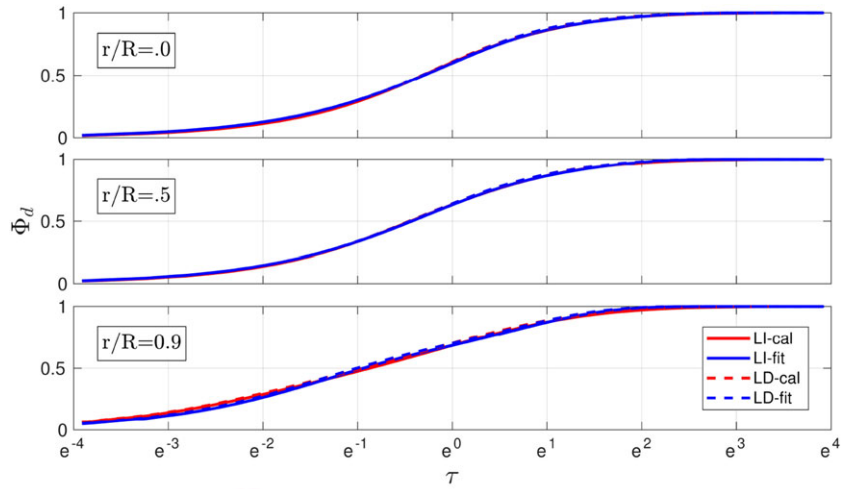

FIGURE 3 Φ_d calculated by the free wake vortex ring (FWVR) and the exponential approximation for baseline $C_t = 0.4$. LI, load increase case; LD, load decrease case [Colour figure can be viewed at wileyonlinelibrary.com]

The coefficients β, ω^1, and ω^2 in Equation (6) are determined for every radial position, all baseline thrust coefficients, and for the load increase and decrease cases. They are obtained by finding the best fit of the indicial responses calculated by the actuator disc vortex models and the indicial function given by Equation (6). The fitting error, ie, the difference between the calculated data and the fitting values and defined by Equation (7)

$$error = 100 * \frac{\Phi_d(r_j, t)_{cal} - \Phi_d(r_j, t)_{fit}}{\Phi_d(r_j, t \to \infty)_{cal} - \Phi_d(r_j, t = 0)_{cal}} \quad [\%], \tag{7}$$

is minimised, where $\Phi_d(r_j, t)_{cal}$ and $\Phi_d(r_j, t)_{fit}$ are the calculated values from the vortex models and the fitted values at the radial position r_j at time t, and where $\Phi_d(r_j, t = 0)_{cal}$ and $\Phi_d(r_j, t \to \infty)_{cal}$ are the calculated values for the two steady states before and after the load change.

In Figures 2 and 3, an example is presented. Figure 2 shows the induction calculated from the VTM model and the exponential approximation of the indicial response at three radial positions ($r/R = 0$, $r/R = 0.5$, and $r/R = 0.9$) for a baseline thrust of $C_t = 0.4$. Figure 3 compares the calculated values from the FWVR model and the exponential approximation at the same radial positions and baseline thrust. The maximum fitting error for all calculated load cases is 3.2% (in the region of $0 \leq r/R < 1$) and 3.5% (in the region of $0 \leq r/R \leq 0.95$) for the VTM and the FWVR model, respectively.

2.3 | Coefficients of the indicial functions

The coefficients β, ω^1, and ω^2 are found to significantly depend on the radial position and the baseline thrust. The coefficients β, ω^1, and ω^2 are therefore represented by a third-order polynomial approximation depending on the radial position. The parameters of the polynomials a_0 to a_3 depend on the baseline thrust coefficient. The coefficients for the load increase and decrease case are averaged to one value and thus no longer one more variable in the expressions. The radial distribution of the coefficients of β, ω^1, and ω^2 obtained by the VTM model are represented by Equation (8). For the FWVR model, they are represented by Equation (9). Different formulae are used for β and ω^1 for the VTM and the FWVR model due to the intrinsic difference between the linear and nonlinear models. The parameters a_3, a_2, a_1, and a_0 for β, ω^1, and ω^2 are given in Table 1.

	VTM			FWVR		
	β	ω^1	ω^2	β	ω^1	ω^2
a_3	38.9	$-3.1C_t - 6.2$	$0.1C_t + 0.1$	$0.36C_t - 0.36$	$2.13C_t^2 - 2.7C_t + 0.77$	$0.05C_t - 0.14$
a_2	−50.3	$5.0C_t + 9.4$	$0.4C_t + 0.7$	$-1.07C_t + 1.09$	$-3.45C_t^2 + 4.74C_t - 1.67$	$-0.18C_t + 1.03$
a_1	−2.9	$-0.3C_t - 0.6$	$-0.1C_t - 0.1$	$0.28C_t - 0.22$	$-0.33C_t + 0.2$	$0.14C_t - 0.14$
a_0	17.2	$-2.4C_t - 3.8$	$-0.5C_t - 0.7$	$0.57C_t + 0.04$	$0.16C_t - 0.32$	$-0.21C_t - 0.75$

TABLE 1 The parameters for the radial distribution of β, ω^1, and ω^2 obtained from the VTM and the FWVR model

Abbreviations: FWVR, free wake vortex ring; VTM, vortex tube model.

VTM model:
$$\beta(r) = 1/(a_3 r^3 + a_2 r^2 + a_1 r^1 + a_0 r^0)$$
$$\omega^1(r) = 1/(a_3 r^3 + a_2 r^2 + a_1 r^1 + a_0 r^0) \cdot$$
$$\omega^2(r) = 1/(a_3 r^3 + a_2 r^2 + a_1 r^1 + a_0 r^0)$$

$$(8)$$

FWVR model:
$$\beta(r) = a_3 r^3 + a_2 r^2 + a_1 r^1 + a_0 r^0$$
$$\omega^1(r) = a_3 r^3 + a_2 r^2 + a_1 r^1 + a_0 r^0 \quad .$$
$$\omega^2(r) = 1/(a_3 r^3 + a_2 r^2 + a_1 r^1 + a_0 r^0)$$

$$(9)$$

More details on how these parameters are obtained are given in Appendix C. The appendix includes information on the radial distributed β, ω^1, and ω^2 and the relationship between a_3, a_2, a_1, and a_0 on one hand and the baseline thrust on the other hand. The quality of the polynomial representation of the results from the VTM and FWVR model is also considered. It is, for example, explained that β is independent from the baseline thrust and not well approximated at the tip region for the VTM. Also, the tip region is highly influenced by the cut-off radius used in the FWVR model, which is not fully captured by the fitting curves.

2.4 | Duhamel integral and its differential form

2.4.1 | Background of Duhamel integral

Duhamel integral is used to calculate the response of a linear system to an arbitrary time-varying external perturbation. If a linear system is initially at rest in an equilibrium position, a unit impulse force is applied at $t = \tau$, $\tau \neq 0$. The response of the linear system to the unit impulse can be written as

$$h(t - \tau) = \frac{1}{I\omega_d} e^{-\zeta\omega_n(t-\tau)} \sin(\omega_d(t - \tau)), \quad t > \tau, \tag{10}$$

where I, ζ, ω_n, and ω_d represent the inertia, the damping ratio, the undamped natural angular frequency, and the damped natural angular frequency of the linear system. The relationship between the damped and undamped natural frequency is given by $\omega_d = \omega_n\sqrt{1 - \zeta^2}$.

The total response of the linear system to an arbitrary applied force, $F(t)$, can be obtained by integrating the series of impulse response. Equation (11) is known as Duhamel integral

$$x(t) = \int_0^t F(\tau)h(t - \tau)d\tau. \tag{11}$$

Further details regarding the derivation of the impulse response and Duhamel integral can be found in the book of Inman.[18]

2.4.2 | Application of Duhamel integral to an actuator disc

The application of Duhamel integral in this paper is under the assumption that the induction response of an actuator disc model to an arbitrary force can be built up as a superposition of responses to a series of step changes in the induction. It is known from the momentum theory ($C_t = 4a(1 - a)$) that the induction of an actuator disc is nonlinear with respect to the thrust, and the nonlinearity increases as the thrust increases. The assumption to use Duhamel integral is thus challenged by high thrust.

If the strength of the vortex tube is a general function $\gamma(t)$, $t \geq 0$ and since the indicial function $\Phi_d(r, t)$ is known, the induced velocity at the disc plane $u_d(r, t)$ by the wake of an actuator disc can be written in terms of Duhamel integral as Equation (12).

$$u_d(r, t) = 0.5\left[\gamma(0)\Phi_d(r, 0) + \int_0^t \frac{d\gamma}{d\sigma}\Phi_d(r, t - \sigma)d\sigma\right]. \tag{12}$$

The relationship between the strength of the generated vortex tube segment γ and the thrust C_t at time t is given in Equation (13).

$$\gamma(t) = V_0(\sqrt{(1 - C_t(t))} - 1). \tag{13}$$

For any known thrust variation, the induced velocity field can be calculated directly using Duhamel integral of the indicial functions analytically or numerically henceforth. However, in the practical operations, the thrust variation is usually unknown in advance. It varies based on wind

conditions and control strategy, which is determined based on the performance of the previous step. Therefore, Duhamel integral should be transformed into a differential form, in order to be implemented in a time marching code such as the BEM code.

Substituting Equation (6) into Equation (12), we get

$$u_d(r,t) = 0.5 \left[\int_0^t \frac{d\gamma}{d\sigma} d\sigma - \int_0^t \frac{d\gamma}{d\sigma} \beta_j e^{\omega_j^1(t-\sigma)} d\sigma - \int_0^t \frac{d\gamma}{d\sigma}(1-\beta_j)e^{\omega_j^2(t-\sigma)} d\sigma \right], \tag{14}$$

and let

$$c_j^n(t) = \int_0^t \frac{d\gamma}{d\sigma} A_j^n e^{\omega_j^n(t-\sigma)} d\sigma, \tag{15}$$

where $n = 1, 2$, and $A_j^1 = \beta_j$, $A_j^2 = 1 - \beta_j$. Differentiating Equation (15) with respect to time t gives

$$\dot{c}_j^n(t) - \omega_j^n c_j^n(t) = A_j^n \dot{\gamma}(t), \quad n = 1, 2. \tag{16}$$

Therefore, the final induced velocity at the actuator disc can be represented by Equation (17).

$$u_d(r,t) = 0.5 \left[\gamma(t) - c_j^1(t) - c_j^2(t) \right]. \tag{17}$$

3 | VERIFICATION METHOD

3.1 | Actuator disc CFD model

To verify all the engineering models, the flow field of an actuator disc is computed. The actuator disc model is constructed in OpenFOAM. A 2D transient solver for incompressible flows is used, namely, pisoFoam. The predefined thrust coefficient is realized by defining uniformly distributed volume forces over the actuator disc region. No turbulence model is applied. The domain has size $[-100D, 100D]$ in width and height. The grid is constructed using blockMesh and is decomposed into a set of one million hexahedral blocks. The grid is dense around the actuator disc and gradually becomes more course away from the disc. The time step is set to $0.0025\frac{V_0}{R}$. This combination of grid and time step has shown to produce converged results. Figure 4 verifies the numerical results from the CFD model against the momentum theory relations between thrust and axial induction for steady uniformly loaded thrust. As it shows, the CFD model is in great agreement with the momentum theory for low thrust. The discrepancy is slightly larger for the highest thrust $C_t = 0.9$, though it is still acceptable. For the unsteady calculations, the initial conditions are defined using the solution of the steady case with a similar baseline thrust.

3.2 | Load cases and data analysis method

The verification is performed using predefined harmonically time-varying load cases, as schematically shown in Figure 5. Two baseline thrusts are defined as $C_t = 1/9$ and $C_t = 7/9$. The amplitude of the harmonic load is set to $\Delta C_t = 1/9$. For the baseline thrust of $C_t = 1/9$, the thrust varies in the range of 0 to 2/9 and provides a relatively low induction. For the baseline thrust case of $C_t = 7/9$, the thrust varies in the range of 6/9 to 8/9. This case provides a larger induction and is closer to the design region at which a wind turbine normally operates. The frequency is
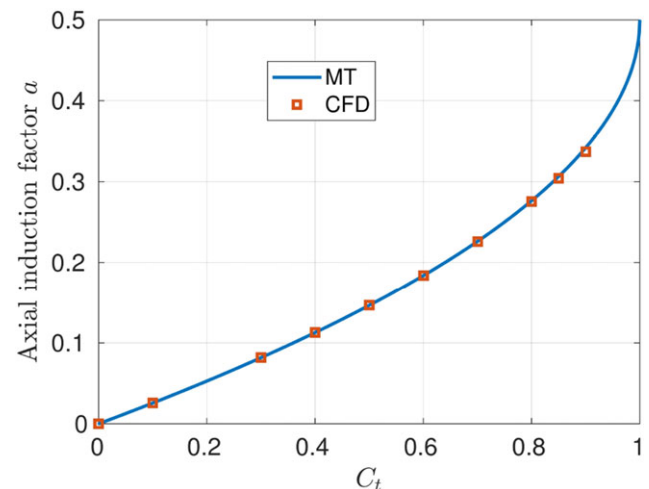

FIGURE 4 Axial induction factor a against C_t calculated from momentum theory and CFD model [Colour figure can be viewed at wileyonlinelibrary.com]
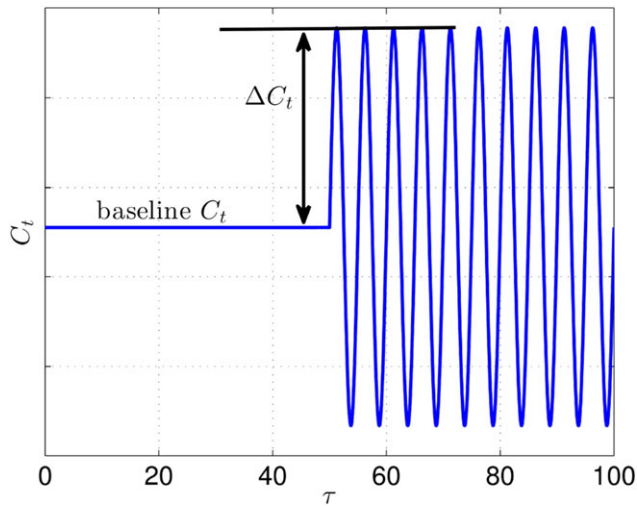
FIGURE 5   Illustration of harmonically time-varying load, $k = 0.2$ [Colour figure can be viewed at wileyonlinelibrary.com]
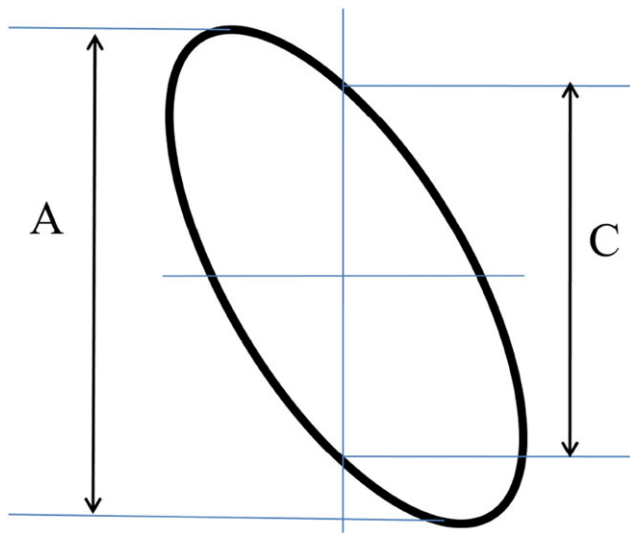

FIGURE 6   Lissajous figure; A, amplitude; C, zero cross height [Colour figure can be viewed at wileyonlinelibrary.com]

nonnormalized using $k = \frac{\omega D}{2V_0}$. Four different reduced frequencies of $k = 0.05, 0.2, 0.5,$ and 1.0 are tested for each baseline thrust. The reduced frequency of $k = 0.2$ is plotted as an example in Figure 5.

In order to quantify the hysteric response of the different models, the amplitude and phase delay are calculated from the hysteresis loop using Lissajous graphic method.[19] Figure 6 shows an example of a Lissajous figure, where A is the velocity amplitude and C is the zero crossing height. The phase difference between the velocity and thrust is

$$\Delta\theta = -[180° - \sin^{-1}(C/A)]. \tag{18}$$

The phase difference between the velocity and the induction is $180°$; the phase difference between the thrust and the induction is $0°$ for the momentum theory. Therefore, the phase delay between the induction from each model and the induction from momentum theory can be calculated by

$$\Delta\theta = -[180° - \sin^{-1}(C/A)] + 180° = \sin^{-1}(C/A). \tag{19}$$

4 | RESULTS AND DISCUSSIONS

The new engineering dynamic inflow models using coefficients obtained by the indicial responses derived from the linear and nonlinear actuator disc vortex models are verified against the numerical results of the CFD model for the load cases introduced in Section 3. They are also compared against the existing engineering models of Pitt-Peters, Øye, and ECN. Further details of these three engineering models are given in Appendix A. In this actuator disc application, the engineering models are integrated using the momentum theory for each annulus. The actuator disc is divided into 100 annuli for all the cases. The thrust is uniformly distributed along the rotor span. It is given as a prescribed input to all the models, which then provide the radial distributed inductions in time as output. In order to obtain a stable induction, the data are recorded after three periods for

all the models. The difference of phase delay between the acquired cycle and the previous one is lower than 1×10^{-2} degree for all models and all frequencies. In the next sections, the velocity at the actuator disc center and the radial distribution of velocity are compared for all models.

Hereinafter, the following names are used when referring to the different models:

MT	momentum theory
MT+P-P	momentum theory integrated with the Pitt-Peters model
MT+Øye	momentum theory integrated with the Øye model
ECN	the ECN model
TUD-VT	the new model based on the linear VTM
TUD-VR	the new model based on the nonlinear FWVR model
CFD	the CFD model implemented in OpenFOAM

4.1 | Velocity at the actuator disc center

Figures 7 and 8 compare the hysteresis loops of the normalized axial velocity at the actuator disc center between the seven models for the baseline $C_t = 1/9$ and $C_t = 7/9$, respectively. The axial velocity at the center of the actuator disc (v_{root}) is subtracted by the steady value (v_{steady}) before normalizing to the free stream velocity (V_0). As shown in all these figures, the velocity at the center of the actuator disc predicted by the Pitt-Peters model goes to MT since the "apparent mass" goes to zero for zero area.

Several general observations can be drawn from Figures 7 and 8. A larger frequency leads to a larger phase delay and a larger difference in amplitude from the steady values. This is a consequence of a higher unsteadiness for a larger frequency. A higher baseline thrust results in a larger amplitude of velocity variation for the same amplitude of thrust variation. This results from the nonlinear relationship between induction and thrust, as discussed in Section 2.4. The difference of all the engineering models from the CFD model is larger for the lowest frequency of $k = 0.05$ than for other frequencies. One main reason for this is that all the engineering models disregard the viscous effects in the developing wake.

For the lower baseline thrust $C_t = 1/9$ in Figure 7, the amplitude of the induction variation is low. In general, the induction at the actuator disc center predicted by all the models is in good agreement with that from the CFD model. Only the difference between the ECN model and the
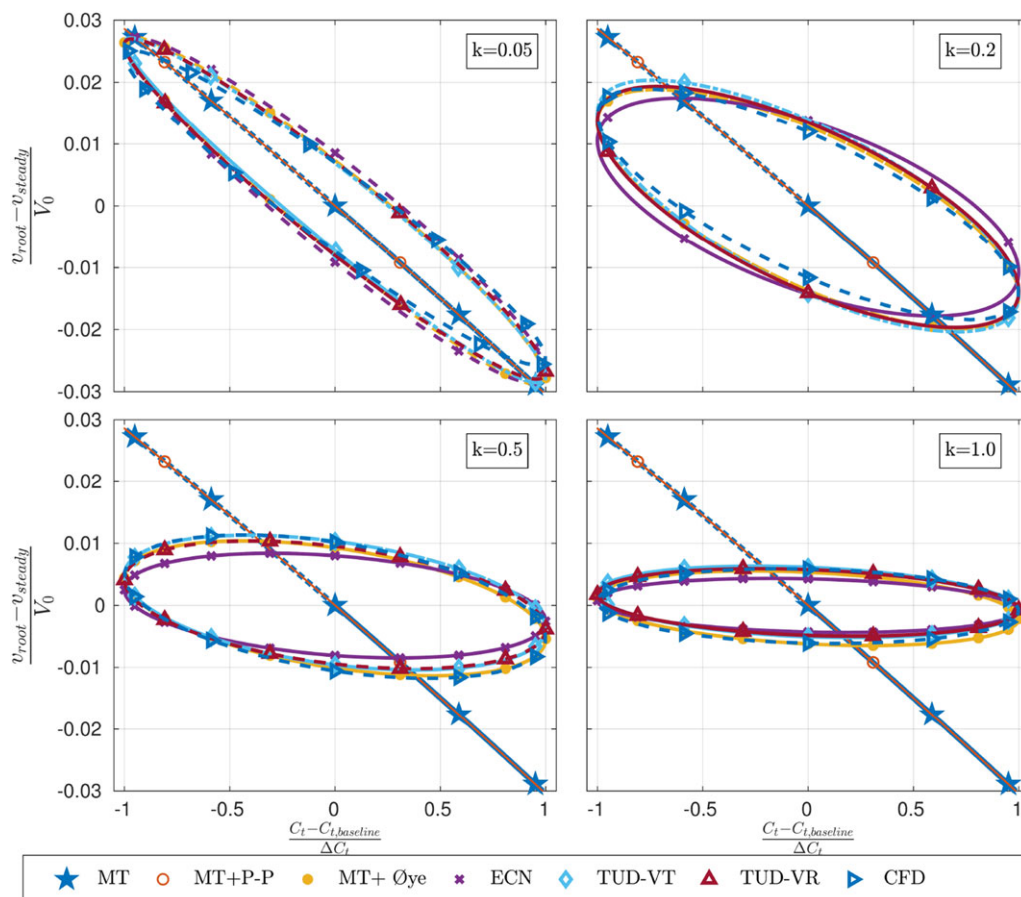

FIGURE 7 Comparison of hysteresis loops of the normalized axial velocity at $r/R = 0$ between the seven models for an actuator disc undergoing harmonic thrust oscillations for baseline $C_t = 1/9$ with an amplitude of $\Delta C_t = 1/9$, for $k = 0.05, 0.2, 0.5$, and 1 [Colour figure can be viewed at wileyonlinelibrary.com]
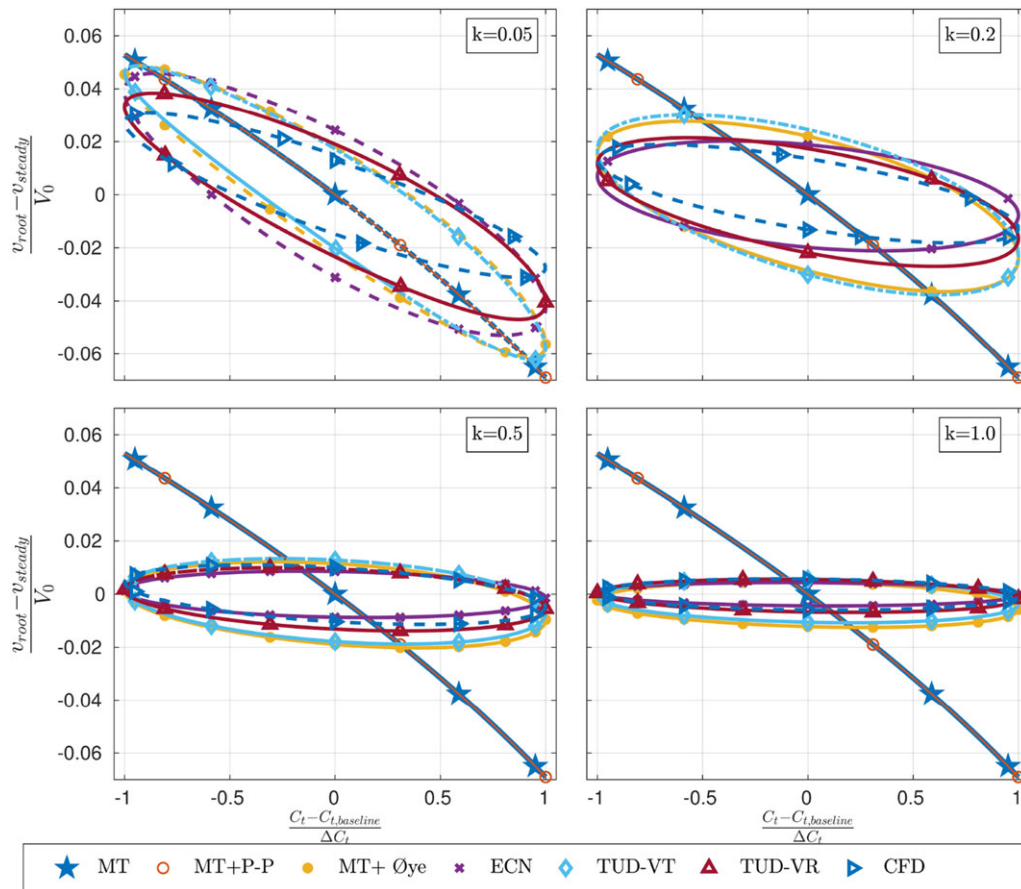
FIGURE 8 Comparison of hysteresis loops of the normalized axial velocity at $r/R = 0$ between the seven models for an actuator disc undergoing harmonic thrust oscillations for baseline $C_t = 7/9$ with an amplitude of $\Delta C_t = 1/9$, for $k = 0.05, 0.2, 0.5$, and 1 [Colour figure can be viewed at wileyonlinelibrary.com]

CFD model is slightly larger for medium frequencies of $k = 0.2, 0.5$. The difference between the two new models of TUD-VT and TUD-VR is small for this low thrust, where the wake expansion effect is low.

For the higher thrust $C_t = 7/9$ in Figure 8, the difference between the engineering models of ECN, Øye, TUD-VT, TUD-VR, and the CFD model is larger than that of lower thrust. The TUD-VT model is closer to the prediction from the Øye model than the others for all the frequencies. The TUD-VR model is closest to the CFD model for all the frequencies.

In order to quantify the results, Figure 9 compares the calculated amplitude and phase delay of the velocity at the actuator disc center between the different models. The amplitude is normalized to the amplitude of the induction from the momentum theory. As seen in Figure 9, the amplitude from MT is constant and the phase delay is zero for all frequencies, owing to the quasi-steady assumption in the model. The ECN model overestimates the phase delay compared with the CFD model for low frequencies of $k = 0.05, 0.2$, and 0.5. The models of TUD-VT and Øye are in good agreement for both phase delay and amplitude for all the cases, which is consistent with Figures 7 and 8. The phase delay from the TUD-VT model agrees with that from the TUD-VR model for both the low and high thrust. However, the amplitude predicted by the TUD-VR model is much closer to the CFD results than that from the TUD-VT model for higher thrust. In general, the TUD-VR model has a better performance considering all the cases with all frequencies in terms of both the phase delay and the amplitude of the velocity at the actuator disc center. The discrepancy between the TUD-VR model and the CFD model is larger for the amplitude at higher thrust $C_t = 7/9$.

4.2 | Radial velocity distribution

The amplitude and phase delay of the velocity from all the models at various radial positions on the actuator disc are investigated in this section. Figures 10 and 12 present the radial distribution of the amplitude and phase delay of the velocity at the actuator disc between the seven models for frequencies $k = 0.05, 0.2, 0.5$, and 1 and baseline thrust $C_t = 1/9$ and $7/9$, respectively. Figures 11 and 13 display the root mean square (RMS) values of amplitude and phase delay of radial distributed velocity between the CFD model and the other six engineering models, for baseline $C_t = 1/9$ and $7/9$, respectively.

The first observation from Figures 10 and 12 is that the distribution of the amplitude and phase delay of the velocity from the Pitt-Peters model shows a reverse trend compared with all the other models. However, this difference cannot be disclosed by evaluating the overall performance, eg, in Yu et al,[8] even though it showed that the performance of the Pitt-Peters model is worse than the models of Øye. The dynamic-inflow
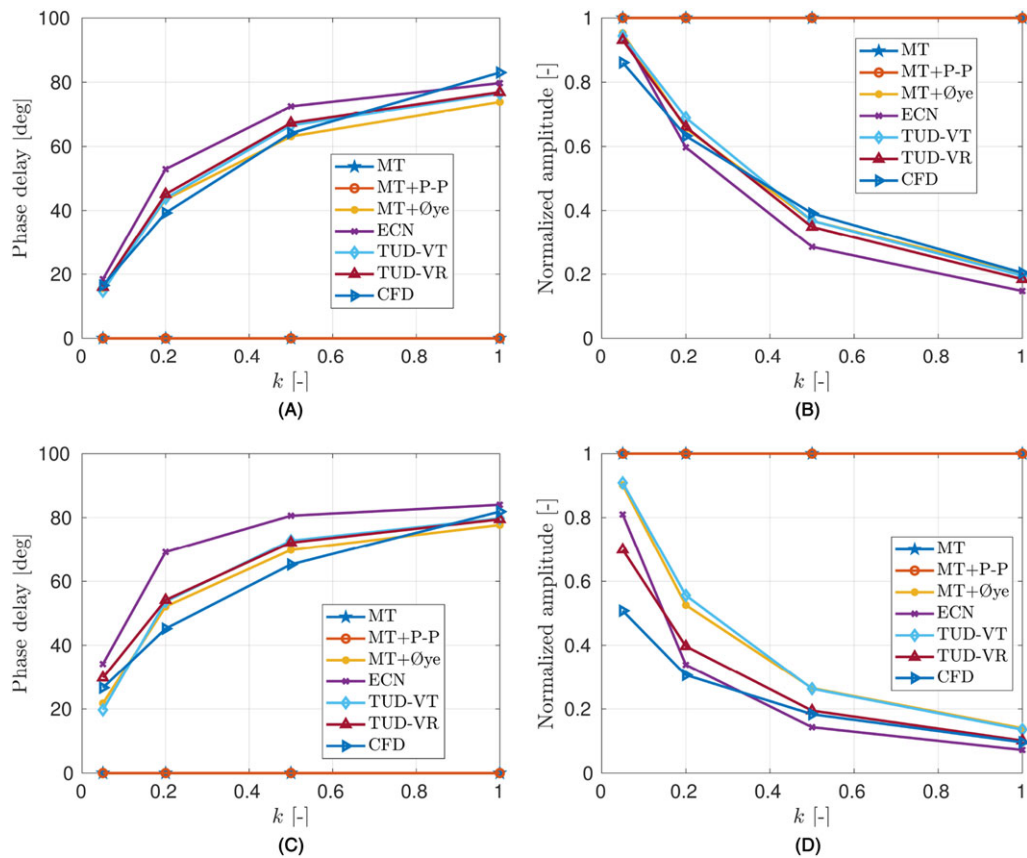
FIGURE 9 The phase delay and amplitude of the velocity at the disc center for baseline $C_t = 1/9$ (top row) and 7/9 (bottom row) [Colour figure can be viewed at wileyonlinelibrary.com]
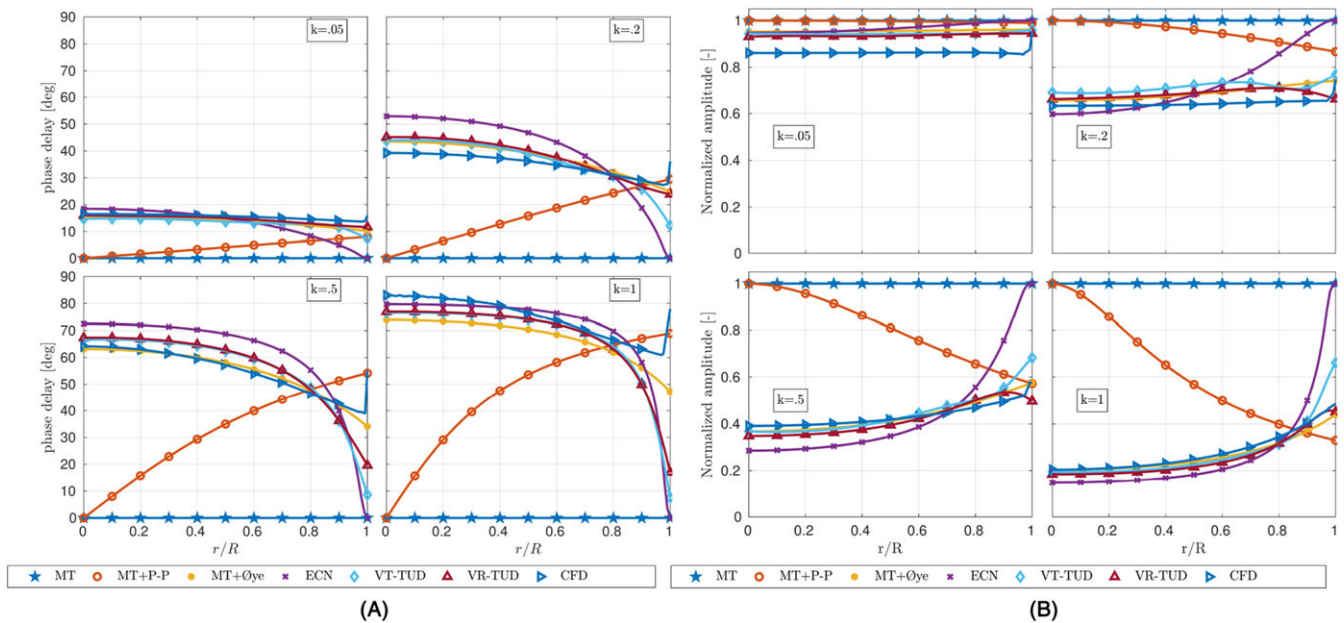

FIGURE 10 Comparison of the radial distribution of the phase delay and amplitude between the seven models for baseline $C_t = 1/9$, for frequencies of $k = 0.05, 0.2, 0.5, 1$ [Colour figure can be viewed at wileyonlinelibrary.com]

model of Pitt-Peters, which is based on the apparent mass theory, cannot predict the radial distribution of the dynamic-inflow effect correctly. This crucial discrepancy was not explored before because most of the previous research focused on the overall loads, eg, the moment at the blade root. The distribution of the dynamic-inflow effect was investigated rarely in literature.[10,20,21]

The difference between all the engineering models and the CFD results in both the phase delay and the amplitude is larger near the tip. This shows that all the engineering models can be improved for dynamic induction at the tip.
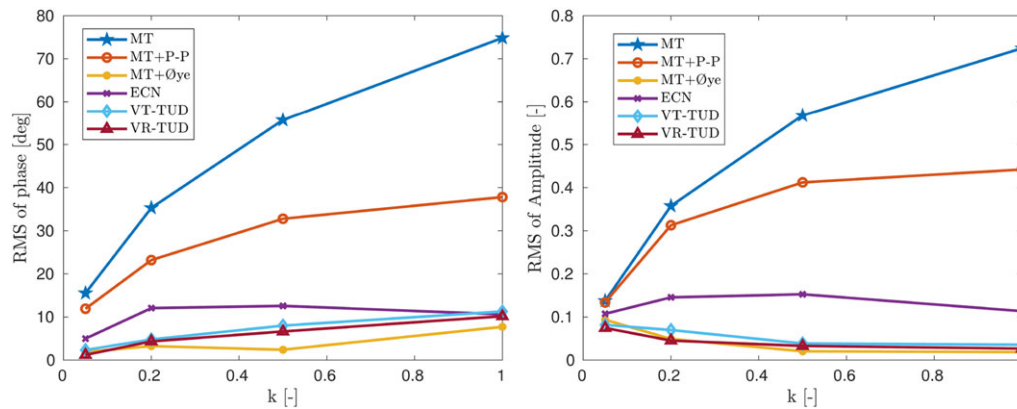
FIGURE 11 Root mean square (RMS) of the phase delay and amplitude between the CFD model and the other engineering models for baseline $C_t = 1/9$ [Colour figure can be viewed at wileyonlinelibrary.com]
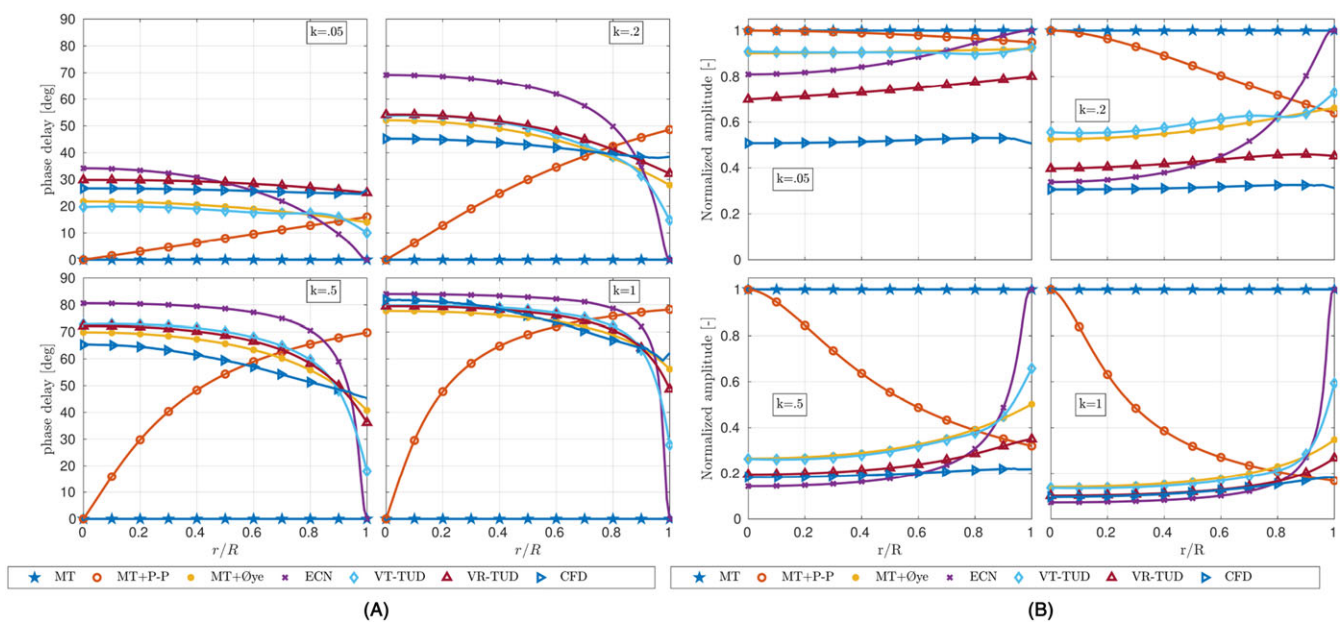

FIGURE 12 Comparison of the radial distribution of the phase delay and amplitude between the seven models for baseline $C_t = 7/9$, for frequencies of $k = 0.05, 0.2, 0.5, 1$ [Colour figure can be viewed at wileyonlinelibrary.com]

As seen in Figures 8-13, the TUD-VT model behaves closely to the Øye model for the value at the root as well as the radial integrated RMS for all load cases, even though the radial dependency is different. The radial dependency is taken into account by Equation (A5) in the Øye model. The Øye model takes into account the wake expansion while the TUD-VT model does not. Their close results can be explained by the fact that both models use two time constants to capture the dynamic induction. Using two time constants is also found to be better than using only one or three terms to predict the dynamic induction (see Appendix B), where it is explained that the flow at the actuator disc is found to decay at two different speeds, a fast one and a slow one, determined by the near wake and far wake, respectively.

For most of the load cases, the prediction of the values at the root and of the radially integrated RMS values by the TUD-VT model is closer to the CFD model than the ECN model. Both the TUD-VT and ECN model are based on a linear actuator disc model; however, two time constants are used in the TUD-VT model while only one time constant is used in the ECN model. The phase delay and amplitude from the ECN model approach the steady value at the tip, resulting in a sharper transient in the tip region than observed in other models. This is determined by the radial dependency factor in this model, which is defined by Equation (A7). This sharp transient at the tip also results in a larger RMS value from the CFD results in Figures 11 and 13.

As seen in Figures 12 and 13, the phase delay predicted by the TUD-VR model is slightly closer to the CFD results than the phase delay of the TUD-VT model. However, the amplitude predicted by the TUD-VR model is much closer to the CFD results. This is because the phase delay is mainly determined by the convection speed of the wake, which is a second-order effect of the wake expansion. However, the wake expansion has a larger effect on the absolute induction at the disc. The wake expansion is larger at higher thrust, and this is neglected by the TUD-VT model.

Figure 11 shows that the RMS value of the phase delay predicted by the Øye model is smaller than that of the TUD-VR model at high frequencies of $k = 0.5$ and 1.0. This is due to the worse performance of the TUD-VR model at the tip region, as shown in Figure 10. Close RMS
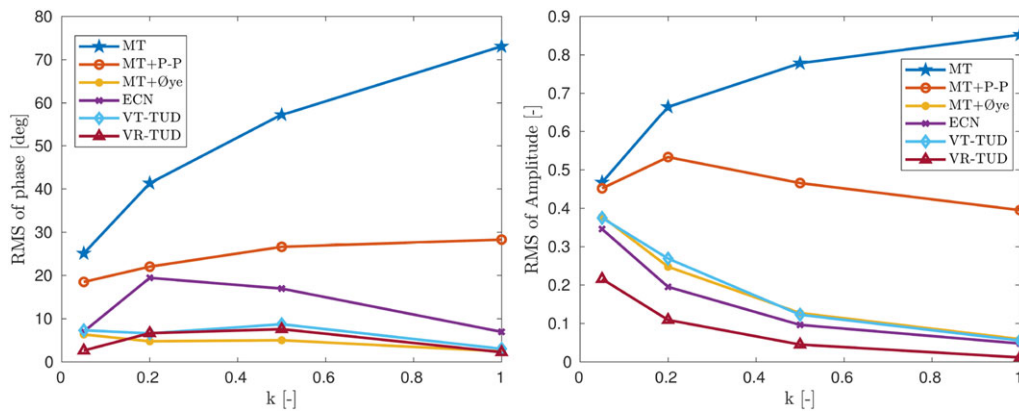
FIGURE 13 Root mean square (RMS) of the phase delay and amplitude between the CFD model and the other engineering models for baseline $C_t = 7/9$ [Colour figure can be viewed at wileyonlinelibrary.com]

values of the phase delay from the two models can also be seen at high thrust in Figure 13. However, the amplitude predicted by the TUD-VR model is much closer to the CFD results than the Øye model for high thrust. This can be caused by the fact that the empirical wake expansion[7] used to obtain the Øye model underestimates the wake expansion at high thrust.

The comparison of all the engineering models shows that the wake expansion is an important aspect to be taken into account to predict the amplitude of the dynamic induction, especially at high thrust. The convection of the wake determines the phase delay of the dynamic induction. The wake convection is influenced by the convection speed of the wake used in all the models and also by the appropriate number of time constant terms to represent the convection characteristic.

As shown in Figures 9, 11, and 13, the difference between the TUD-VR model and the CFD model in phase delay increases as the frequency increases. This is caused by the larger thrust jump δC_t per unit time at large frequencies. A larger thrust jump introduces a larger error in using Duhamel integral. The difference between the TUD-VR model and the CFD model in the amplitude distribution is larger at high thrust (Figure 12) than that for low thrust (Figure 10). This is because the FWVR model itself, from which the TUD-VR model is derived, is challenged at higher thrust. A larger thrust results in an earlier occurrence of the wake instability.[8] This instability is difficult to simulate correctly without the consideration of viscosity or introducing remeshing techniques. This also makes it difficult to model the turbulent wake that is present for high thrust cases. Furthermore, the discretization of the wake by vortex rings may play a role. All these factors can influence the accurate representation of the real wake by the FWVR model.

5 | CONCLUSIONS

In this paper, two new dynamic-inflow engineering models are developed based on the indicial responses of a linear actuator disc vortex model and a nonlinear actuator disc vortex model. Both models use the differential form of Duhamel integral to make the models ready to be implemented in a time marching code like BEM.

Using two time constants is found to be necessary to predict correctly the phase delay of the dynamic induction, which is consistent with previous research.[10] The flow at the actuator disc is found to decay at two different speeds, a fast one and a slow one, which are determined by the near wake and far wake, respectively. The phase delay and amplitude difference of the velocity from all the models (except for the MT) display a strong radial dependency. Better predicting the radial dependency can be an important area to improve the prediction of engineering models, especially at the tip region.

Verification against the CFD model shows that the TUD-VT model, based on the indicial responses of the linear actuator disc vortex model, predicts results close to the Øye model for all the cases. The TUD-VR model, based on the indicial responses of the nonlinear actuator disc vortex model, predicts better results than the other engineering models concerning both phase delay and amplitude, especially at high thrust.

All engineering models are verified against a high-fidelity CFD model for the basic load cases used in this paper. Further validation for more complex load cases by high quality experimental data will give more insight for their application in BEM. The discrepancy between the TUD-VR model and the CFD model suggests that correction for the assumption of linearity in Duhamel integral and including the viscous diffusion effect can be two main points to further improve the engineering models.

Nomenclature

C_t	thrust coefficient (-)
R	radius of the actuator disc (m)
h	the impulse response function of a linear system (-)
x	the total response of a linear system to an arbitrary force (-)
F	the arbitrary force applied to a linear system (N)

γ	the strength of the discretized vortex tube (m s^{-1})
v_{root}	axial velocity at the center of the actuator disc (m s^{-1})
v_{steady}	axial velocity at the center of the actuator disc in steady state (m s^{-1})
v_0	free stream velocity (m s^{-1})
k	reduced frequency ($k = \frac{\omega D}{2V_0}$) (-)
τ	nondimensionalized time ($\tau = \frac{t \cdot V_0}{R}$) (-)
Φ	axial induced velocity field (m s^{-1})
Φ_d	normalized axial induction at the actuator disc plane (-)
u_d	axial induced velocity at the actuator disc plane (m s^{-1})
MT	momentum theory
BEM	blade element momentum method
FWVR	free wake vortex ring model
VTM	vortex tube model
MT+Øye	momentum theory integrated with the Øye model
MT+P-P	momentum theory integrated with the Pitt-Peters model
ECN	the ECN model
CFD	the CFD model implemented in OpenFOAM
TUD-VT	the new model based on the linear VTM model
TUD-VR	the new model based on the nonlinear FWVR model

CONFLICTS OF INTEREST

The authors declare no potential conflict of interests.

ORCID

Wei Yu https://orcid.org/0000-0001-7829-6129

Delphine Tavernier https://orcid.org/0000-0002-8678-8198

REFERENCES

1. Schepers JG. Engineering models in wind energy aerodynamics. *Ph.D. Thesis*: Delft University of Technology; 2012.
2. van Engelen TG, van der Hooft EL. Dynamic inflow compensation for pitch controlled wind turbines. In: European Wind Energy Conference; 2004; London.
3. Snel H, Schepers JG. Joint investigation of dynamic inflow effects and implementation of an engineering method. Tech. Rep., Energy Research Center of the Netherlands; 1995.
4. Schepers JG, Snel H. Dynamic inflow: yawed conditions and partial span pitch control. Tech. Rep., Petten, Energy Research Center of the Netherlands; 1995.
5. Pitt DM, Peters DA. Theoretical prediction of dynamic-inflow derivatives. *Vertica*. 1981;5(1):21-34.
6. Øye S. Unsteady wake effects caused by pitch-angle changes. In: Proceedings of the First IEA Symposium on the Aerodynamics of Wind Turbines; 1986; London:58-79.
7. Øye S. A simple vortex model of a turbine rotor. In: Proceedings of the Third IEA Symposium on the Aerodynamics of Wind Turbines; 1990; Harwell:1-15.
8. Yu W, Ferreira C, van Kuik GAM, Baldacchino D. Verifying the blade element momentum method in unsteady, radially varied, axisymmetric loading using a vortex ring model. *Wind Energy*. 2016;20(2):269-288.
9. Yu W, Hong VW, Ferreira C, van Kuik GAM. Validation of engineering dynamic inflow models by experimental and numerical approaches. *J Phys Conf Ser*. 2016;753(Torque):22024. http://stacks.iop.org/1742-6596/753/i=2/a=022024?key=crossref.a5021875b25c355fb9838721e1c241a3
10. Pirrung GR, Madsen HA. Dynamic inflow effects in measurements and high fidelity computations. *Wind Energy Science*. 2018;3(2):545-551.
11. Wagner H. Über die Entstehung des dynamischen Auftriebes von Tragflügeln. *Zeitschrift für angewandte Mathematik und Mechanik*. 1925;5(1):17-35. http://doi.wiley.com/10.1002/zamm.19250050103
12. Yu W, Ferreira C, van Kuik GAM. Analytical actuator disk solution for unsteady and/or non-uniform loading. In: 34th Wind Energy Symposium; 2016; California:1-12. http://arc.aiaa.org/doi/10.2514/6.2016-0751
13. Branlard E, Gaunaa M. Cylindrical vortex wake model: right cylinder. *Wind Energy*. 2014;18(11):1973-1987.
14. Beddoes TS. Practical computation of unsteady lift. In: Eight european rotorcraft forum; 1982; Aix-en-Provence.
15. Leishman JG. *Principles of Helicopter Aerodynamics*, 2nd ed.. New York: Cambridge University Press; 2006.
16. Branlard E, Gaunaa M. Superposition of vortex cylinders for steady and unsteady simulation of rotors of finite tip-speed ratio. *Wind Energy*. 2015;19(7):1307-1323. http://arxiv.org/abs/1605.01449

17. Jones RT. The unsteady lift of a wing of finite aspect ratio. Tech. Rep., National Advisory Committee for Aeronautics; 1939.

18. Inman DJ. *Engineering Vibrations*. 3rd ed. Upper saddle river: Pearson Education, Inc.; 2009.

19. Al-Khazali HAH, Askari MR. Geometrical and graphical representations analysis of Lissajous figures in rotor dynamic system. *IOSR J Eng*. 2012;2(5):971-978.

20. Hand MM, Simms DA, Fingersh LJ, et al. Unsteady aerodynamics experiment phase VI: wind tunnel test configurations and available data campaigns. Tech. Rep., Colorado, National Renewable Energy Laboratory; 2001.

21. Schepers JG. IEA Annex XX : Dynamic inflow effects at fast pitching steps on a wind turbine placed in the NASA-Ames wind tunnel. Tech. Rep., Petten, Energy Research Center of the Netherlands; 2007.

22. Hansen MOL. *Aerodynamics of Wind Turbines*. 2nd ed. London: Earthscan; 2008.

APPENDIX A: DYNAMIC-INFLOW ENGINEERING MODELS

1. The Pitt-Peters dynamic-inflow model

The Pitt-Peters dynamic-inflow model[5] was developed for an actuator disc with an assumed inflow distribution across the disc. Based on the assumption that the equation of Pitt-Peters can be applied to a blade element or actuator annulus, the dynamic-inflow equation for each annular ring becomes

$$\frac{1}{\rho A_j V_0^2/2}\left[\frac{8}{3\pi}\rho A_j r_j \frac{dv_j}{dt} + 2\rho A_j v_j(V_0 + v_j)\right] = C_{tj}, \tag{A1}$$

where j indicates the jth annular ring, A_j and C_{tj} are the area and thrust coefficient of the jth annulus, and v_j is its azimuthal averaged induced velocity.

2. The Øye dynamic-inflow model

In the Øye dynamic-inflow model,[6,7] the induced velocity is estimated by filtering the quasi-steady values through two first-order differential equations

$$v_{int} + \tau_1 \frac{dv_{int}}{dt} = v_{qs} + b\tau_1 \frac{dv_{qs}}{dt}, \tag{A2}$$

$$v_z + \tau_2 \frac{dv_z}{dt} = v_{int}, \tag{A3}$$

where v_{qs} is the quasi-steady value from blade element momentum (BEM), v_{int} is an intermediate value, and the final filtered value v_z is treated as the induced velocity. After calibration using a vortex ring model,[7] the two time constants are recommended as follows[3]:

$$\tau_1 = \frac{1.1}{(1 - 1.3a)}\frac{R}{V_0}, \tag{A4}$$

$$\tau_2 = \left(0.39 - 0.26\left(\frac{r_j}{R}\right)^2\right)\tau_1, \tag{A5}$$

where a is the axial induction factor, R is the rotor radius, r_j is the radius of jth annulus, and b is a constant value of 0.6.

3. The ECN dynamic-inflow model

The dynamic-inflow model developed by ECN[1,3] was derived from an integral relation of the stream tube model (see more details of the streamtube model in the book of Hansen[22]). For the condition of constant wind speed, the equation is

$$\frac{R}{V_w}f_a \frac{da}{dt} + a(1 - a) = C_{tj}/4, \tag{A6}$$

where C_{tj} is the axial force coefficient of the rotor annulus j. The dynamic-inflow effect in this model is modeled by adding a first-order time derivative of the axial induced velocity to the momentum theory relation. The term f_a is a function of the radial position, defined as

$$f_a = 2\pi/\int_0^{2\pi} \frac{[1 - (r/R)cos\varnothing_r]}{[1 + (\frac{r}{R})^2 - 2(r/R)cos\varnothing_r]^{\frac{3}{2}}}. \tag{A7}$$

APPENDIX B: EFFECT OF DIFFERENT NUMBERS OF EXPONENTIAL TERMS

This section discusses the effect of approximating the indicial functions using different numbers of exponential terms. With one term, the indicial function is approximated using

$$\Phi_d(r_j, t) = 1 - e^{\omega_j^1 t}. \tag{B1}$$

With two terms, the approximation is given by Equation (6), and with three terms, by

$$\Phi_d(r_j, t) = 1 - \beta_j^1 e^{\omega_j^1 t} - \beta_j^2 e^{\omega_j^2 t} - (1 - \beta_j^1 - \beta_j^2) e^{\omega_j^3 t}. \tag{B2}$$

Figure B1 displays the calculated values from the free wake vortex ring (FWVR) model and the exponential approximation using Equations (B1) and (B2) and Equation (6) of the indicial responses of velocity at different radial positions $r/R = 0$, $r/R = 0.5$, and $r/R = 0.9$ for baseline $C_t = 0.4$. It can be seen that using only one exponential term is not sufficient to capture the induction response correctly. The curves are better approximated using two or three exponential terms.

Figure B2 presents the radial distribution of the amplitude and phase delay of the velocity at the actuator disc plane. The numerical results from the FWVR model are compared with the results from the engineering models using coefficients obtained by approximating the indicial functions using Equations (B1) and (B2) and Equation (6), for frequencies $k = 0.05, 0.2, 0.5$, and 1, for baseline $C_t = 7/9$. As expected, the phase
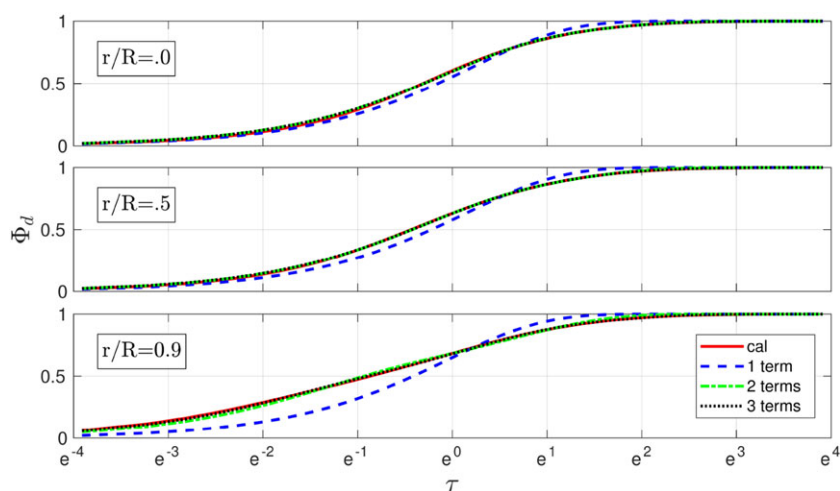

FIGURE B1 Φ_d calculated by the free wake vortex ring (FWVR) and the approximation using one, two, and three exponential terms for baseline $C_t = 0.4$ for load increase case [Colour figure can be viewed at wileyonlinelibrary.com]
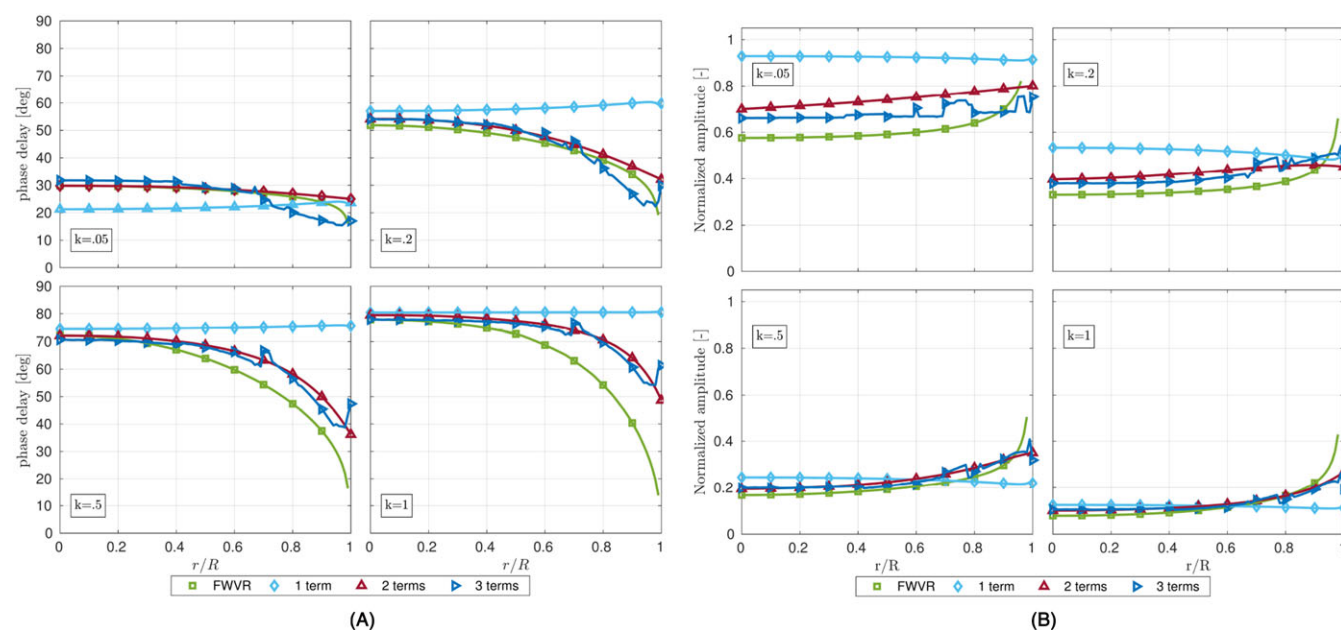

FIGURE B2 Comparison of the radial distribution of the phase delay and amplitude between the free wake vortex ring (FWVR) model and engineering models using coefficients by approximating the indicial functions using one, two, and three exponential terms, for baseline $C_t = 7/9$, for frequencies of $k = 0.05, 0.2, 0.5, 1$ [Colour figure can be viewed at wileyonlinelibrary.com]

and amplitude predicted using the coefficients using one exponential term approximation is worst. It cannot capture the radial distributed trend correctly. The figures further show that using three exponential terms, the approximation is overfitting and becomes irregular.

Tests in this section show that using two terms of exponential is best. Therefore, the models of TUD-VT and TUD-VR are developed by approximating the indicial functions using two terms of exponential series.

APPENDIX C: INDICIAL RESPONSES OF LINEAR AND NONLINEAR ACTUATOR DISC VORTEX MODELS

In this section, the process of obtaining the radial distribution of the coefficients for the indicial functions from the linear and nonlinear actuator disc vortex models is presented.

The linear VTM model: The radial distribution of the coefficients β, ω^1, and ω^2 are represented by polynomials in Equation (8). The fitted and the polynomial representations of the radial distribution of the coefficients of β, $\frac{1}{\omega^1}$, and $\frac{1}{\omega^2}$ for several values of the baseline thrust are shown in Figure C1. As shown, the radial distributed coefficients of β, $\frac{1}{\omega^1}$, and $\frac{1}{\omega^2}$ can be well represented by the polynomials. The parameters of the polynomials in Equation (8) for β, ω^1, and ω^2 are plotted against the baseline C_t in Figure C2. As can be seen from Figures C1 and
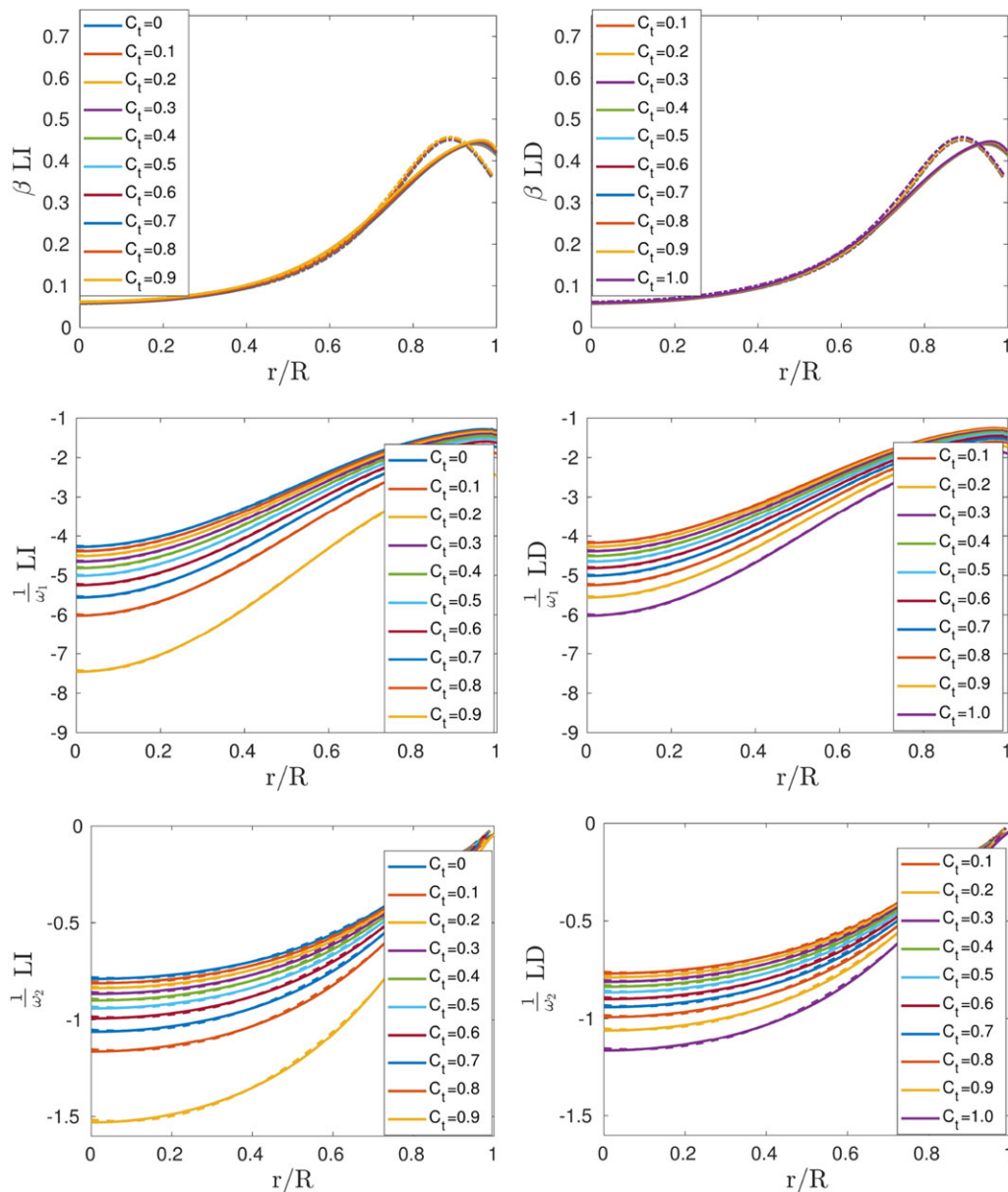

FIGURE C1 The radial distribution of β, $\frac{1}{\omega^1}$ and $\frac{1}{\omega^2}$ of the indicial responses of different baseline C_t from the vortex tube model (VTM) for load increase and decrease cases. Solid lines: fitted coefficients; dashed lines: the polynomial approximation of the radial distribution of coefficients [Colour figure can be viewed at wileyonlinelibrary.com]
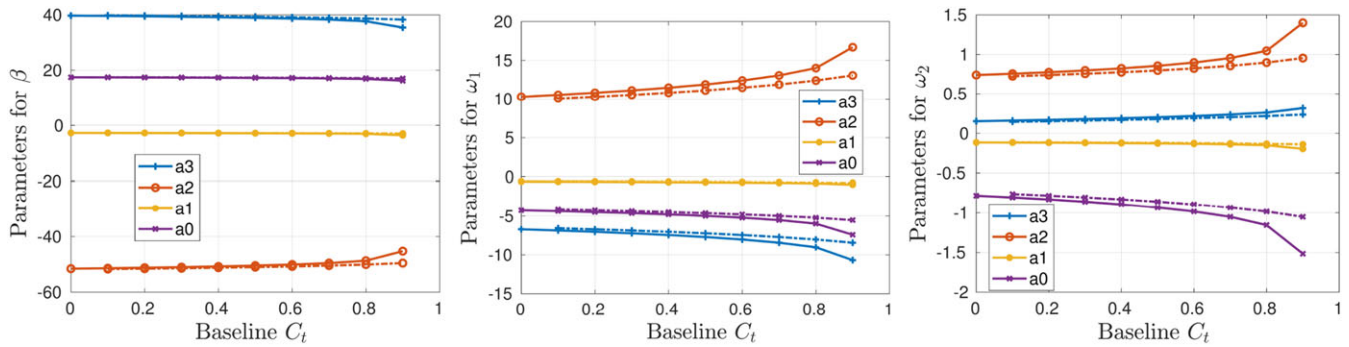
FIGURE C2 The parameters of a_3, a_2, a_1, a_0 for β, ω^1, and ω^2 against C_t from the vortex tube model (VTM). Solid line: load increase; dot-dashed line: load decrease [Colour figure can be viewed at wileyonlinelibrary.com]

C2, the difference between load increase and load decrease cases is small. Therefore, the averaged values of the load increase and decrease cases are used. Figure C2 shows that the distribution of β obtained by the VTM is independent from C_t. Only small difference exists when C_t is close to 1. The parameters of a_3, a_2, a_1, and a_0 for ω^1 and ω^2 against C_t are represented by a first degree polynomial. The final used parameters are given in Table 1.

The nonlinear FWVR model: The process of obtaining the radial distribution of the coefficients for the indicial functions from the nonlinear actuator disc vortex model is the same as for the linear model. The radial distribution of the coefficients β, ω^1, and ω^2 for the FWVR model is represented by polynomials in Equation (9). The fitted and the polynomial representations of the radial distribution of the coefficients of β, $\frac{1}{\omega^1}$, and $\frac{1}{\omega^2}$ of different baseline thrust values are shown in Figure C3. It shows that the values obtained by the FWVR model are strongly affected by the cutoff radius used in the tip region, which is not fully captured by the polynomial representation. Excluding the region $r/R > 0.95$, the radial distributed coefficients can be well represented by the polynomial. The parameters for β, ω^1, and ω^2 from the FWVR model are plotted against the baseline C_t in Figure C4. As seen from Figures C2 and C4, the difference for the distributed coefficients between load increase and decrease load cases obtained by the nonlinear FWVR model is larger than that from the linear VTM. The parameters of a_3, a_2, a_1, and a_0 for ω^1 and ω^2 against C_t are also obtained based on the averaged value between the load increase and decrease cases. These final used values are given in Table 1.

The quality of using the polynomial approximation of the coefficients is analyzed for both the VTM and the FWVR model. A difference is observed mainly at the tip region. The maximum root mean square (RMS) value of amplitude and phase delay of the radially distributed velocity for the FWVR between using the polynomial approximated coefficients and using the fitting coefficients is 0.024 and 3.0°, respectively, within the region $r/R \leq 0.95$. The corresponding maximum RMS of amplitude and phase delay for the VTM model is 0.027 and 1.2°, respectively.

Comparison between Figures C1 and C3 shows that the distributed parameters from the FWVR model and from the VTM model are close as thrust approaches 0, attributing to the small wake expansion at low thrust. However, the difference is not only caused by the small wake expansion but also by the different convection speed used in the two models. An empirical convection velocity is used for the VTM, while the induced velocity from the entire wake and the incoming flow are considered for the convection in the FWVR model. As shown in Figures 2 and 3 and Figures C1 and C3, the unsteady flow responses from both models can be well represented using two terms of exponential series. These two terms embody two speeds of flow decay, a fast decay and a slow decay. The slow decay, represented by $\frac{1}{\omega^1}$, is determined by the far wake while the fast decay, represented by $\frac{1}{\omega^2}$, is determined by the near wake. Therefore, β and (1-β) represent the proportion of the contributions to induction from the far wake and the near wake, respectively. Comparison between Figures C1 and C3 further shows that the baseline thrust has a negligible impact on the coefficient β for the VTM. For the FWVR model in Figure C3, β and $\frac{1}{\omega^1}$ are highly influenced by the baseline thrust, but the thrust has a slighter impact on $\frac{1}{\omega^2}$. In the linear VTM model, the wake geometry does not change radially when the thrust changes, resulting in the same β for different baseline thrust. In the nonlinear FWVR model, the wake geometry changes radially so the distance of the vorticity to the actuator disc plane also changes radially, resulting in different radial distributions of β for different baseline thrust. For both the VTM and the FWVR model, a larger baseline thrust leads to a larger induction, which means a smaller convection velocity of the vortex elements. This results in slower decay speed from both the far wake and the near wake, which is reflected by the decrease of $\frac{1}{\omega^1}$ and $\frac{1}{\omega^2}$ for an increase of baseline thrust.
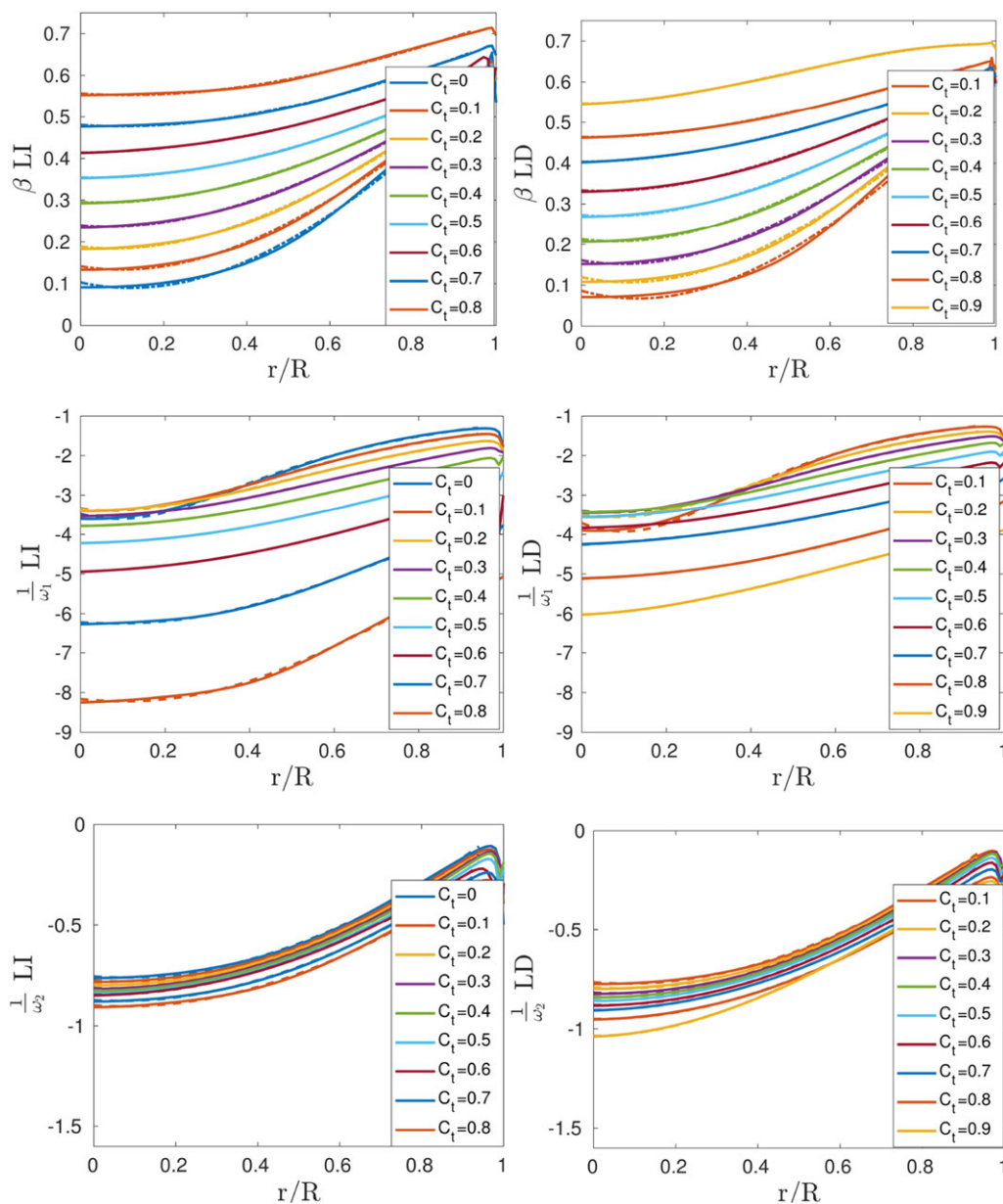
FIGURE C3 The radial distribution of β, $\frac{1}{\omega^1}$, and $\frac{1}{\omega^2}$ of the indicial responses of different baseline C_t from the free wake vortex ring (FWVR) model. Solid line: fitted coefficients; dashed line: the polynomial approximation of the radial distribution of coefficients [Colour figure can be viewed at wileyonlinelibrary.com]
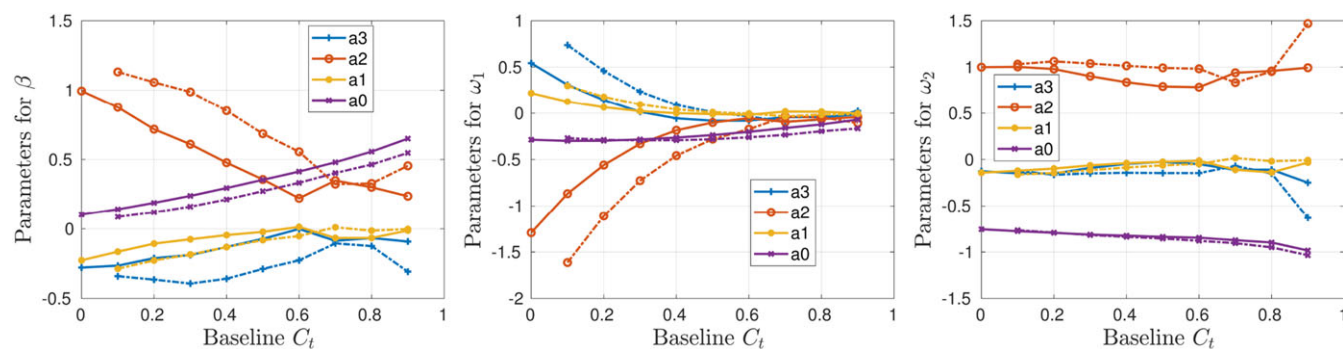

FIGURE C4 The parameters of a_3, a_2, a_1, a_0 for β, ω^1, and ω^2 against C_t from the free wake vortex ring (FWVR) model. Solid line: load increase; dot-dashed line: load decrease [Colour figure can be viewed at wileyonlinelibrary.com]